Evaluating the impact of a late-burial corrosion model on reservoir permeability and performance in a mature carbonate field using near-wellbore upscaling

Chandra, Viswa Santhi shanti; Wright, Paul; Barnett, Andrew; Steele, Richard; Milroy, Paul; Corbett, Patrick William Michael; Geiger-Boschung, Sebastian; Mangione, Alessandro

Published in:
Fundamental Controls on Fluid Flow in Carbonates

DOI:
10.1144/SP406.11

Publication date:
2015

Evaluating the Impact of a Late-burial Corrosion Model on Reservoir Permeability and Performance in a Mature Carbonate Field Using Near-wellbore Upscaling

*Viswasanthi Chandra[1, 2], Paul Wright[3], Andrew Barnett[3], Richard Steele[3], Paul Milroy[3], Patrick Corbett[1, 2], Sebastian Geiger[1, 2], Alessandro Mangione[1, 2]

1. Institute of Petroleum Engineering, Heriot-Watt University, Riccarton, Edinburgh, EH14 4AS, UK.
2. International Centre for Carbonate Reservoirs
3. BG Group, 100 Thames Valley Park, Reading, RG6 1PT, UK.
*Corresponding author (e-mail: viswa.chandra@pet.hw.ac.uk)

Number of words: 6061
Abbreviated Title: Impact of late-burial corrosion on reservoir permeability

Abstract

Field X comprises a giant Palaeogene limestone reservoir with a long production history. An original geomodel used for history matching employed a permeability transform derived directly from core data. However, this permeability model required major modifications, such as horizontal and vertical permeability multipliers, in order to match the historic data. The rationale behind these multipliers is not well understood and not based on geological constraints. Our study employs an integrated near-wellbore upscaling workflow to identify and evaluate the geological heterogeneities that enhanced reservoir permeability. Key among these heterogeneities are mechanically weak zones of solution-enhanced porosity, leached stylolites and associated tension-gashes, which were developed during late stage diagenetic corrosion. The results of this investigation confirmed the key role of diagenetic corrosion in enhancing the permeability of the reservoir. Insights gained from the available production history, in conjunction with petrophysical data analysis, substantiated the characterisation of this solution-enhanced permeability. This study provided valuable insights to the means by which a satisfactory field-level history match for a giant carbonate reservoir can be achieved. Instead of applying artificial permeability multipliers that do not necessarily capture the impacts of geological heterogeneities, our method incorporates representations of fine-scale heterogeneities. Improving the characterisation of permeability distribution in the field provided an updated and geologically consistent permeability model that could adequately contribute to the ongoing development plans to maximize incremental oil recovery.

1. Introduction: The giant carbonate Field X

Field X is a giant offshore oil and gas field with a long production history from a limestone reservoir. Permeability has been identified as one of the biggest uncertainties associated with the reservoir simulation model during field optimisation studies that have been carried out by the operator previously. A reduction in the uncertainties for the permeability distribution is needed to evaluate the feasibility of the next development phase.

In this study we attempt to resolve these issues through a systematic re-evaluation of the reservoir simulation model, considering, in particular, the field's diagenetic history. Our aim is to understand the fundamental controls on fluid flow that need to be adequately captured in the reservoir model. Geological studies carried out by the operator suggest that the key permeability pathways are strongly related to the mechanism of reservoir poro-perm evolution during late-burial corrosion (Wright & Barnett 2011). Late-burial corrosion in Field X is referred to as deep burial/mesogenetic corrosion associated with the corrosion of limestone by burial-derived (hypogene) fluids. However, it is unclear how a diagenetic model that accounts for late-burial corrosion should be included in the reservoir simulation model and how such an updated reservoir simulation model could impact production forecasting. In this study we first describe the multi-scale geological and petrophysical heterogeneities caused by late-burial corrosion. We then discuss a new small-scale and high-resolution reservoir modelling approach, which is based on near-wellbore modelling and upscaling. The high-resolution modelling enables us to evaluate these heterogeneities to incorporate them in the reservoir simulation model. Finally, we analyse the sensitivity of simulated cumulative fluid production profiles to several model scenarios that incorporate new permeability distributions that have been guided by near-wellbore upscaling results.

1.1 Permeability modelling challenges in Field X

The permeability model, used for reservoir simulation and history matching of Field X, was obtained solely by using the permeability transform from core data (Figure 1), which constrains the average reservoir permeability to be 20 mD. However, over 25 years of production history supports an interpretation of a stratiform high-permeability network with horizontal permeability on the order of 200 mD. Core recovery was poor as significant parts of the reservoir comprise high-permeability and probably mechanically weak carbonates, which have been altered by mesogenetic corrosion. Hence the recovered core plugs suffer from inherent sample bias and the resulting core analysis hardly sampled any high-permeability carbonates. Yet, such high-permeability carbonates are clearly apparent in the dynamic data.

Because core sampling was biased to lower permeability values, the reservoir simulation model required major modifications to obtain a satisfactory history match. These modifications were exclusively of numerical nature, comprising, for example, horizontal permeability multipliers of x10 and x20 in the main reservoir zones. In addition, vertical permeability, local well permeability and productivity index (PI) multipliers were also needed. Although collectively these lead to a good history match, it appears that the “right” history match was achieved for the “wrong” geological reason. Removing the different permeability multipliers causes the quality of the history match to degrade significantly (Figure 2). This suggests that the original geomodel permeability is inadequate although it can be calibrated using artificial multipliers; but these are not based on geological constraints. Numerous studies, supported by a steady water-cut profile over the field’s long production history (Figure 3), indicate that a connected natural fracture network is probably absent in Field X (Oates et al. 2012).

Two key questions for evaluating future development scenarios are hence: What is the geological nature of the high-permeability zones that are required in the reservoir simulation model to obtain an adequate history match? How can we quantify and represent these zones to update the reservoir simulation model in a geologically consistent way rather than using artificial multipliers? Our hypothesis is that the enhanced permeability in Field X was caused by late-burial corrosion and this needs to be accounted for in the geomodel. We employ a novel near-wellbore upscaling workflow (Chandra et al. 2013) to assess and incorporate the multi-scale geological features arising from late-burial corrosion more reliably in the field-scale reservoir model.

1.2 Database for Field X

Over 300 meters of core from 4 vertical wells and 1 highly deviated pilot well in Field X were inspected for this study. For petrophysical evaluation, we used Routine Core Analysis (RCA) and Special Core Analysis (SCAL), along with high resolution images of the core and thin-sections from all these wells. In addition, two wells have probe-permeameter data from core slabs and we have measured apertures for stylolites and dissolution seams. Core Spectral Gamma Ray logs, wellbore image logs and the typical well-log suite containing Gamma Ray, Density-Porosity and Sonic logs were used as well.

The original geological-petrophysical model of Field X and the history matched simulation model were provided by the operator and serve as the base case throughout this study. The geomodel grid was constructed in a North-South direction. It comprises over five million grid blocks with cell dimensions of 50 m x 50 m horizontally. The model contains a total of 59 layers. Cell sizes in the vertical direction have an average thickness of 2 m, enabling the resolution of reservoir layers and the capture of vertical heterogeneity. The reservoir simulation model contains a total of 170 wells, of which over 80 are horizontal multi-lateral wells. Production data is available for over 25 years.

1.3 Geological setting of Field X

Field X and the basin that contains it are part of a bigger structure that is a pericratonic rift basin (Goswami et al. 2007). The latter is an offshore, divergent passive continental margin basin that was formed due to extensional tectonics during Late Jurassic-Early Cretaceous period with NW-SE-trending horst-graben geometry (Goswami et al. 2007). Earlier studies indicate that this rifting was followed by moderate subsidence during the Late Cretaceous, leading to the development of widely spread carbonate platforms. Carbonate deposition occurred as a series of shallowly dipping clinoforms representing stacked facies belts prograding into the basin. Within this regional setting, Field X comprises an Eocene-Oligocene limestone reservoir, which has a broad, low-relief anticlinal trap structure. The overburden to the reservoir comprises offshore mudstone and limestone. The reservoir is currently at its maximum burial depth (about 1700 m) and may also be at its maximum temperature of 130˚C.

The two main hydrocarbon bearing zones in Field X are the Early Oligocene A Zone and Eocene B Zone (Figure 4), which are continuous across the field. The reservoir contains an oil rim about 20 meters thick below a gas column of up to 50 meters. The oil rim is being produced through a gas cap drive mechanism (Oates et al. 2012). The main reservoir zones are interpreted to be highstand systems tracts and their stratigraphic framework is summarized as a stacked depositional sequence in a distally steepened shallow ramp setting (Figure 5). The predominant lithofacies in the field are nodular packstones and wackestones intercalated by grainstones. A Zone is dominated by *Nummilitides* while B Zone limestones mainly contain an assemblage dominated by *Coskinolina*. The biota and facies associations indicate that the A Zone records more distal sedimentation on the ramp than the B Zone. The two zones are separated by a disconformity that shows evidence of sub-aerial exposure and erosion in core corresponding to an early Oligocene fall in relative sea level. A shale unit overlying this disconformity records a substantial transgression to mid-ramp facies in the A Zone and acts as transient local seal, capping the B Zone.

1.4 Diagenesis and reservoir quality in Field X

The main controls of porosity and permeability in Field X have been discussed by Wright & Barnett (2011). They are summarised in Figure 6 and discussed briefly below. Following deposition, the sediments of the B Zone were stabilised and cemented under shallow burial conditions while the A Zone underwent deeper phreatic stabilisation. It is thought that porosity remained low in the A Zone during intermediate burial phase while the B Zone went through extensive compaction and pressure dissolution. Stylolites, microstylolites and clay seams developed ubiquitously during intermediate burial. The majority of the stylolites are associated with tension-gashes, some of which were cemented (Moshier 1989; Alsharhan 1990; Alsharhan & Sadd 2000). Although the Eocene B Zone was exposed subaerially during the early Oligocene and a few cored wells show short intervals of cemented karst breccia, there is no widespread diagenetic signature of this event in the reservoir.

Both A and B zones clearly show the effects of a major phase of mesogenetic dissolution prior to hydrocarbon arrival (Figures 7-9). It appears that the stylolites and associated tension-gashes were opened by a tectonic uplift event and conducted reactive fluids containing sulphides, silica and aluminium, enabling them to migrate into the surrounding host matrix. These reactive fluids corroded the formerly tight cemented matrices by selectively removing the micritic grains having high surface area (Wright & Barnett 2011). The conduits feeding the reactive fluids to the reservoir are not known with certainty. Feed through faults and from the closely underlying basement are both possible. The presence of exotic minerals in the core such as pyrite, dickite and saddle dolomite supports mixing corrosion mechanism as defined by Esteban et al. (2003).

Numerous studies have demonstrated that mesogenetic dissolution is a key control for reservoir quality in other carbonate reservoirs worldwide (e.g. Mazzullo & Harris 1991; Jameson 1994; Esteban & Taberner 2002, 2003; Sattler et al. 2004; Lambert et al. 2006). Even though some authors (Ehrenberg et al. 2012) have questioned this, it is therefore widely accepted that burial corrosion can extensively alter the static and dynamic properties of a reservoir, for example porosity, permeability, relative permeability and wettability. Most likely, reservoir quality in Field X is also significantly controlled by this late-burial corrosion, impacting formation porosity over several orders of magnitude in scale, varying from seismic-scale breccia pipes to strongly fabric selective micro-porosity (Wright &Barnett 2011).

The B Zone is dominated by inner ramp *Coskinolina* grainstones to packstones, which developed high amplitude stylolites and associated fractures. These allowed the corrosive fluids to selectively remove the fine grained walls of agglutinated miliolid foraminifera in the early phase of corrosion. During later phases, the sparite and more coarsely crystalline foraminifera were extensively corroded. In contrast, there was only weak development of stylolites in the outer ramp *Nummulitic* packstones and wackestones of A Zone due to a higher clay content that prevented the formation of high amplitude stylolites (Wright & Barnett 2011). Hence the millimetre-sized clay seams and microstylolites caused only low to moderately intense corrosion, which resulted in widespread micro-porosity development in these formerly tight cemented limestones. Note that micro-porosity in Field X is defined as pores with a pore throat diameter of 2 microns or less.

In summary, the main present-day porosity types and probably the majority of the reservoir porosity, originated as a result of late-burial corrosion of A and B Zone limestones, caused by the arrival of burial-derived (hypogene) fluids. The key porosity types are leached stylolites and associated tension-gashes, solution-enhanced intergranular and vuggy macroporosity, and microporosity (Figure 8). Microporosity was created as a leached microporous mosaic, associated with solution-enhanced intercrystalline porosity grading into larger pores (Wright & Barnett 2011). In the following sections, we refer to the intervals that contain the porosity types listed above as Corrosion Enhanced Porosity (CEP) zones. Hence, the CEP zones comprise well-connected micro- and macro-pore networks with leached stylolite and tension-gash porosity, all of which act as a high-permeability network that significantly enhances fluid flow in the reservoir.

1.5 Petrophysical description and evaluation of the CEP zones

Table 1 summarises the assessment of the CEP zones based on the available petrophysical data. Over 300 metres of well cores were inspected to obtain detailed core description of the CEP zones, including the spatial and structural aspects of the leached stylolites and tension-gashes. Observations from core and thin-sections indicate that the stylolites are Type III stylolites. Type III stylolites are high amplitude and anastomosing stylolites (Aharanov et al. 2012). These stylolites are frequently associated with vertical to sub-vertical tension-gashes (Figure 9). These features are typically leached and coexist with extensive solution-enhanced micro- and macro-porosity halos. These are the CEP zones (Figure 8).

As noted earlier, the available core plug data suffers from sample insufficiency arising from poor core recovery of high-porosity CEP zones as they are probably mechanically weaker. This resulted in a sample bias towards the uncorroded tight limestone. Although the core plug data by itself failed to characterize the permeability distribution in the CEP zones effectively, the core slabs still could be used to obtain probe-permeameter data. However, probe-permeameter measurements are sensitive to the local pore geometries because of the small sample size of such measurements (Corbett et al. 1999). Hence these measurements need to be evaluated with care as the CEP zones comprise a variety of solution-enhanced porosity types, including moldic, vuggy and stylolite porosities.

In addition to the above factors, neither core plug nor the probe-permeameter data could measure porosity and/or permeability values for the leached stylolites and tension-gashes. Previous studies suggest that stylolites are often localised and laterally extensive planar surfaces (e.g. Peacock & Azzam 2006; Ebner et al. 2010; Koehn et al. 2012). Stylolites are also bound by rough-walled, non-planar surfaces (e.g., Renard et al. 2004; Brouste et al. 2006). Using the idealised assumption that stylolites are bound by two planar and smooth surfaces, we have calculated the permeability range of the stylolites and tension-gashes based on their apertures from the parallel plate law (Witherspoon et al. 1980). This law implies that for laminar flow between two fracture walls, the, fracture permeability, K, is proportional to the fracture aperture, a, squared, and can be estimated as $K= a^2/12$. Although this law makes the highly idealised assumptions that fracture walls are smooth and planar, studies have shown that the parallel plate law can provide reasonable permeability estimates for rough-walled and non-planar fracture surfaces with highly heterogeneous flow fields (Dijk et al. 1999). Another important assumption in the parallel plate law is that the fractures remain open. However, in Field X we observe that stylolites and tension-gashes can be partially filled with dickite and bladed calcite (Figure 7c). Dickite is a high-temperature phyllosilicate clay mineral and was precipitated in Field X as a bi-product of mesogenetic dissolution (Wright & Barnett 2011). The impact of dickite and calcite on fracture permeability is unknown and requires further investigation. A further challenge is that apertures measured in the stylolites and tension-gashes at surface conditions are most likely different from the apertures at reservoir conditions. We hence have used a heuristic approach and reduced the aperture values initially measured in the core by a factor of 10. Subsequently we have also analysed the impact of apertures ranging from 0.01 to 0.02 mm. In summary, the permeability of the stylolites and tension-gashes is associated with uncertainty related to the roughness of the stylolite surfaces, the overburden/unloading effect on the apertures and the local precipitation of dickite and calcite within the stylolites and tension-gashes. The uncertainty in permeability of the stylolites and tension-gashes impacts the upscaled horizontal and vertical permeabilities that are computed in our near-wellbore modelling workflow. We analyse these sensitivities in the later sections when we use the minimum and maximum apertures to obtain the corresponding range of effective permeabilities from our near-wellbore upscaling workflow.

The core description logs were used in conjunction with the core plug and probe-permeameter data to estimate porosity and permeability of the CEP zones in the wells. The wireline porosity log was also used to validate the estimated porosity distribution for the CEP zones. The range of porosity and permeability values in the CEP zones that were obtained from Routine Core Analysis (RCA) and well log data is listed in Table 2. The CEP zones typically displayed higher porosity values (Figure 10). The probe-permeameter values measured in the CEP zones show permeabilities that are over two orders of magnitude higher relative to those from the surrounding unaltered limestone (Figure 11). Even considering the aforementioned uncertainties in permeability measurements for complex pore types (Corbett et al. 1999), this difference is significant and indicates that the CEP zones are likely a primary control for fluid flow in Field X.

Image logs can be correlated readily with core and probe-permeameter data and they confirm the presence and extensive distribution of the corroded zones throughout the well (Figure 12). The dark conductive patches on the Formation Micro-Image log were consistent with the CEP zones, which in turn correspond to higher mini-permeameter measurements on the core. In contrast, light coloured resistive patches indicate the tight limestone.

2. Near-wellbore modelling and upscaling workflow

The wide-spread occurrence of CEP zones in Field X is likely to be a key control for fluid flow in Field X. However, as mentioned before, due to sample bias towards the low-permeability tight limestones, the CEP zones are currently not included in a geologically consistent way in the reservoir simulation model. Instead, different permeability multipliers were introduced until a satisfactory history match was achieved. Hence an accurate re-evaluation of the horizontal permeability K_h for the CEP zones is needed. Considering the drive mechanism in Field X where the oil rim is produced by expanding the gas cap (Oates et al. 2012), it is expected that the ratio of vertical to horizontal permeability, K_v/K_h, needs to be modelled accurately in Field X to capture the main flow mechanisms. It is therefore crucial to disentangle and understand how the different solution-enhanced porosity types in the CEP zones, from micro-porosity to leached stylolites and tension-gashes, impact reservoir permeability individually and cumulatively.

We approach this challenge using a systematic modelling and upscaling workflow in which we employed near-wellbore modelling tools. Near-wellbore modelling can estimate the effects of geologically realistic millimetre to decimetre scale geological features on permeability (Wen et al. 1998; Nordahl 2004; Elfenbein et al. 2005; Nordahl et al. 2005; Ringrose et al. 2008; Chandra et al. 2013). They also allow us to evaluate how small-scale heterogeneities impact reservoir-scale flow behaviours by incorporating them in sector- and field-scale reservoir models. Chandra et al. (2013) demonstrated that near-wellbore modelling tools can be used to simulate the impact of small-scale geological heterogeneities in a highly heterogeneous clastic reservoir and that the inclusion of these heterogeneities in field-scale models leads to better calibrated reservoir models.

We used a commercial near-wellbore modelling software, SBED™, to obtain realistic reservoir property distributions for the millimetre to centimetre-sized geological features in the CEP zones. SBED™ creates models of the small-scale heterogeneities in which surfaces and volumes are generated through a process-oriented modelling approach that involves the recreation of sedimentary processes by migrating sine functions (Wen et al. 1998; Nordahl 2004). It is also possible to overprint the depositional structures in these models with diagenetic features such as using object modelling (Dabek & Knepp 2011; Chandra et al. 2013). This results in high-resolution unstructured porosity and permeability grids with cell volumes less than 1 cm^3. These grids describe the small-scale heterogeneities. Their effective permeabilities can be readily computed using flow based, single-phase upscaling with mixed-finite element methods (Wen et al. 1998; Chandra et al. 2013). The resulting effective properties are then used as input for reservoir-scale modelling and simulation by mapping them on to the reservoir simulation grid which should be locally refined around the wells (Chandra et al. 2013).

2.1 Modelling CEP zones with near-wellbore modelling tools

We created a range of high-resolution, i.e. centimetre-scale, models with SBED™ that represent the CEP zones (Figure 13). These models also include the leached stylolites (Figure 13a) and associated tension-gashes (Figure 13b). Input data for the near-wellbore modelling came from the detailed core description, petrophysical analysis, and probe-permeameter data described above.

Figure 13c illustrates a near-wellbore modelling scenario in which stylolites are surrounded by solution-enhanced matrix porosity halos. The spatial and geometrical parameters of the leached stylolites and the vertical to sub-vertical tension-gashes were based on the core observations. The near-wellbore model dimensions were selected such that the multi-scale heterogeneities were adequately represented while the resulting K_v/K_h values were appropriate for the reservoir geomodel. The model dimensions for the near-wellbore modelling workflow were $\Delta X = \Delta Y = \Delta Z = 20$ cm. The cell dimensions were $\Delta x = \Delta y = 0.2$ cm. This allowed us to represent the size of the leached stylolites and tension-gashes realistically. The cell dimension in the z-direction, Δz, varied between 2 mm to 1 cm, depending on the vertical dimension of the geological structures that we needed to resolve. Porosity and permeability statistics that are needed as input for the near-wellbore modelling were obtained from the probe-permeameter and core plug data. In this way, multiple scenarios of CEP zone models could be generated. These models include or exclude stylolites and tension-gashes. We also varied the density of distribution of the stylolites and tension-gashes and evaluated how different apertures could impact their permeabilities using the minimum and maximum apertures of 0.01 mm and 0.02 mm respectively.

2.2 Upscaling the near-wellbore models to obtain effective properties for the CEP zones

The near-wellbore models of the small-scale heterogeneities in the CEP zones were upscaled in SBED™ to compute the effective porosity, horizontal permeability and K_v/K_h values using flow-based upscaling. A pressure solver method with periodic and open boundary conditions (Pickup & Sorbie 1996) was used to estimate a more realistic effective full-permeability tensor for the small-scale heterogeneities. The resulting upscaled properties show that the effective horizontal permeability is significantly improved in the CEP zones, i.e. when the solution-enhanced micro- and macro- porosity in the matrix, leached stylolites and the tension-gashes are accounted for. Effective permeabilities ranged from 1 to 350 mD for solution-enhanced micro- and macro-porosity model scenarios. This is in stark contrast to the original core derived permeability which varied from 0.01 to 50 mD. If stylolites and associated tension-gashes are included, the upscaled permeability can be as high as 1000 mD. Including stylolites and tension-gashes also increased the vertical permeability considerably and leads to K_v/K_h ratios that can be as high as 2.5. The models that only account for corrosion-enhanced matrix porosity yield K_v/K_h ratios of up to 1. In this context, we note that the K_v/K_h ratio in the original geomodel was a uniform 0.1. Table 3 lists the typical upscaling results for all modelled near-wellbore scenarios and indicates that the leached stylolites and associated tension-gashes can act as a highly permeable network in conjunction with the surrounding solution-enhanced matrix porosity.

3. Translating near-wellbore modelling-derived permeabilities in the CEP zones to reservoir permeability

Effective permeabilities estimated for the high-resolution near-wellbore models clearly show an increase in permeability in the CEP zones for all model sensitivities. However, these effective permeabilities are still well below the scale of a reservoir simulation grid block and it is hence necessary to translate them to the reservoir simulation grid block scale so as to evaluate how the small-scale permeability enhancement impacts reservoir-scale fluid flow.

We approach the above issue by comparing the effective near-wellbore modelling-derived porosity and horizontal permeability values for the different models in the CEP zones, i.e. models that include or exclude stylolites and tension-gashes, with the porosity-permeability transform derived from the core plug data. We use Lucia's (1995 and 1999) class 1, 2 and 3 porosity-permeability transforms at the core plug scale, as shown in Figure 14. The original porosity-permeability values measured on the plugs follow Lucia's class 3, which indicates a lower reservoir quality. In contrast, effective porosities and permeabilities from the near-wellbore models of the CEP zones follow Lucia's class 2, indicating much better reservoir quality. This increase in K_h and K_v/K_h associated with Lucia's class 2 transform indicates that the "missing" permeability enhancement in the original reservoir model could be recovered using a different permeability-porosity transform; that is, applying Lucia's class 2 transform may overcome the need to use permeability multipliers to increase fluid flow in the reservoir simulation model in order to achieve an adequate history match. It must be noted that although Lucia's class 2 transform matches the effective near-wellbore modelling-derived permeability-porosity data well, it only accounts for interparticle porosity, i.e. strictly speaking it does not account for fracture or "touching vug" porosity. While it would be possible, in principle, to derive a new permeability-porosity transform for Field X using only near-wellbore modelling and upscaling, along with other data such as well-tests and plug measurements, this is beyond the scope of the work presented here. We hence proceed with Lucia's class 2 transform to translate porosities measured at the wireline-log scale to permeabilities, and use these values to update the geological and reservoir simulation models. This approach resulted in new permeability distributions in the geomodel, all of which were guided by near-wellbore modelling and upscaling. These new geomodels account for different combinations of small-scale heterogeneities in the CEP zones. As these models incorporate additional geological information for the CEP zones, we expect that they should lead to more reliable forecasts of hydrocarbon production and should require less artificial permeability multipliers.

Since Field X requires a large and complex simulation model (Figure 15a) that requires considerable computing time, we only update the geomodels for a sector model containing Well Group 1 (Figure 15b). Well Group 1 was selected because it is the well group with the longest production history. It consists of 12 vertical and 11 horizontal production wells. There were approximately 376,000 active cells in the sector model. Each cell has an average dimension of $\Delta X = \Delta Y = 50$m and average thickness of $\Delta Z = 1$ m in B Zone and $\Delta Z = 2$ m in A Zone.

The original geomodel, without its permeability multipliers, served as the base case. Recall that this geomodel comprises a permeability distribution that is biased towards the low-permeability, uncorroded matrix. To generate additional geomodel scenarios that represent various late-burial corrosion heterogeneities, we introduced a reservoir rock typing approach and defined rock type R1 as the tighter uncorroded matrix and rock type R2 as the highly permeable CEP zone. This is in contrast to the original geomodel which did not contain a facies model or any rock types. Rock type R2 was varied to reflect the different small-scale heterogeneities that are observed in the CEP zone. That is, R2 contains varying combinations of solution-enhanced matrix porosity, leached stylolites and tension-gashes, expressed through variations in effective permeability and porosity as computed from the near-wellbore modelling and upscaling.

Rock type logs of R1 and R2 were generated for the near-wellbore region of the wells using available core description. These logs provided density and porosity cut-offs based on the petrophysical log analysis, which allowed us to generate additional rock type logs for the wells without core. These rock type logs were then upscaled into the reservoir grid blocks using weighted averaging. Sequential Indicator Simulation (SIS) (Deutsch & Journel 1998; Deutsch 2002) was used to distribute R1 and R2 away from the wellbore. The porosity distribution was calculated for each model using Sequential Gaussian Simulation (SGS) (Deutsch & Journel 1998; Deutsch 2002) based on the wireline porosities and conditioned to our new rock type distributions. Multiple model scenarios were obtained by varying the lateral correlation lengths of the rock type R2.

For the base case, we used the porosity-permeability transform from the original core data, i.e. the transform that was biased towards a tighter rock matrix and is similar to Lucia’s class 3 transform (Figure 14). The same transform was also used to calculate permeability within rock type R1. Lucia’s class 2 porosity-permeability transform was tested for rock type R2 and was found to represent the permeabilities derived from the near-wellbore modelling and upscaling of the heterogeneities in the CEP zones more closely (Figure 14). The vertical and horizontal permeabilities from the near-wellbore modelling and upscaling were used to estimate the respective K_v/K_h ratios for rock type R2. These ratios varied depending on the presence or absence of solution-enhanced micro- and macro-porosity in the matrix, leached stylolites and associated tension-gashes. Over all, this approach resulted in over 25 permeability scenarios, ranging from the original geomodel to geomodels that account for all the heterogeneities observed in the CEP zones. This allowed us to simulate a range of production profiles and to analyse how small-scale geological heterogeneities caused by late-burial corrosion impact the dynamic behaviour of Field X. It also allowed us to investigate if a geomodel that accounts for the CEP zone can provide better history matches without requiring permeability multipliers.

4. Impact of the CEP zones on reservoir performance

Oil, gas and water production data for the different permeability models were simulated for Well Group 1 (Figure 15b), using the original field development strategy, i.e. we used the same well production scheduling and well-controls as in the history matched model. Only the first 10 years of production were simulated. We then compared the resulting production profiles and evaluated which of the different model scenarios has the smallest misfit, i.e. which of the different model scenarios is most likely because its simulated production profiles agree best with the observed ones.

The base case, i.e. the geomodel without permeability multipliers, displays a cumulative oil production that does not match the observed production at all. This mismatch decreases significantly when rock type R2, and hence the small-scale heterogeneities in the CEP zone, is included into the geomodel (Figure 16). This indicates that the permeability multipliers in the history match were only needed to recover the “missing” permeability from rock type R2.

Case 1 and Case 2 in Figure 16 represent two different geomodel scenarios for R2. In both cases the horizontal permeability within rock type R2 was modelled using Lucia’s class 2 transform, i.e. the rock type includes the combined impact of solution-enhanced matrix, stylolite and tension-gashes (Figure 13b). In both cases, rock type R2 was also modelled using a small correlation length of 50 m, which is equivalent to the simulation grid block size. The key difference is that the K_v distribution for rock types R1 and R2 in Case 1 was computed using the uniform K_v/K_h ratio of 0.1 from the base case. In Case 2, however, the K_v/K_h ratio for R2 was taken from the near-wellbore modelling and upscaling. In other words, the improvement of vertical permeability caused by the network of leached stylolites and tension-gashes in conjunction with matrix porosity was not accounted for in Case 1.

Both, Case 1 and Case 2 showed significantly improved matches between the simulated and historic oil production. This was due to the increase in horizontal permeability, which allows for additional flow in the reservoir and hence higher oil production rates. However, simulations for Case 1 failed to obtain a successful match of the simulated gas and water production profiles (Figure 17 and Figure 18). This is due to the reduced K_v/K_h ratio in Case 1. Case 2, which uses the K_v/K_h ratio from the near-wellbore modelling and upscaling, allows for additional flow in the vertical direction and hence represents the vertical fluid displacement caused by the particular drive mechanism in Field X more adequately. Case 2 therefore showed significantly improved matches for the gas (Figure 17) and water production (Figure 18). Rock type R2 with the higher K_v/K_h ratio improved the lateral and vertical connectivity in the reservoir by accounting for leached stylolites and associated tension-gashes as well as the corrosion-enhanced matrix porosity. This inference provided a valuable insight towards the sensitivity of the simulated production profiles in Field X towards the contribution of leached stylolites to the vertical permeability of rock type R2.

Neither Case 1 nor Case 2 could achieve perfect matches to the historic oil production. We suspect that this could have several reasons. First, we only use Lucia's class 2 transform as a proxy to estimate the permeability of rock type R2. As noted earlier, Lucia's transforms do not account for fractures and open touching vugs. A better match for the oil production rate could possibly be obtained by generating a new, tailor-made porosity-permeability transform using our near-wellbore modelling and upscaling approach, as well as the available core data and possibly dynamic data. Secondly, it is likely that the late-burial corrosion could have impacted other properties of Field X such as relative permeability and wettability that will influence, in particular, the oil rates. Lastly, there are other uncertainties such as aquifer strength, PVT properties, or initial fluid distributions that can impact the quality of a history match. However, all these "secondary" uncertainties can now be analysed more readily, thanks to an improved, better calibrated, geologically consistent and hence more reliable geomodel that accounts for the CEP zones. We expect that these updated models will require significantly less modifications and calibration during advanced history matching and uncertainty quantification workflows compared to the original permeability model. Ultimately, this will provide more reliable production forecasts that enable to plan the next development phases for Field X more robustly.

It should be noted that, as a side effect, the elimination of artificial permeability multipliers in the reservoir simulation model also reduced the computing time significantly. This is of additional value as a larger number of simulations can be performed in a smaller time frame when evaluating future field development scenarios, enabling the analysis of a larger parameter space and the quantification of uncertainties in oil production more robustly.

5. Conclusions

We have used a novel near-wellbore modelling and upscaling workflow to evaluate the impact of small-scale geological heterogeneities caused by late-burial corrosion on the reservoir fluid production profiles in a giant offshore carbonate reservoir with a prolonged production history. We have demonstrated, using a re-evaluation of the core data, near-wellbore modelling, and reservoir simulation, that solution-enhanced matrix micro- and macro-porosity, leached stylolites and associated tension-gashes have a significant impact on reservoir permeability and quality. We have created a large number of geomodel cases, each of which contains different combinations and lateral extents of these corrosion enhanced porosity (CEP) zones. Our near-wellbore upscaling results allowed us to incorporate these small-scale heterogeneities in field-scale reservoir simulation models by computing their effective properties from small-scale and high-resolution models.

Fluid production was simulated for the different reservoir models, ranging from the original geomodel to geomodels which incorporate all the small-scale heterogeneities related to the late-burial corrosion. We compared the simulated production profiles with the historic production data to rank the different geological models and evaluate the most likely scenario based on the best match between simulated and observed production data. The smallest mismatch between simulated and historic production profiles was obtained when we not only included an increased horizontal permeability but also related the vertical-horizontal ratio to late-burial corrosion features in the geomodel.

The outcome of this study has led to a significantly improved characterisation of the permeability distribution in the field, which is now much better constrained to the reservoir geology. While the original reservoir simulation model required excessive use of permeability multipliers in order to match the historic production data, our new model has largely eliminated the need for such multipliers. We hence expect that our new model, which accounts for small-scale heterogeneities, will require significantly less efforts to be fully calibrated to dynamic data using advanced (assisted) history matching techniques. Our updated reservoir model is therefore better suited to contribute to the ongoing development plans and help forecast incremental oil recovery more accurately.

We are grateful to Foundation CMG for supporting the PhD project of Viswasanthi Chandra and supporting the Chair of Sebastian Geiger. The BG asset team is thanked for providing the necessary data and support required for the project. We would like to extend our thanks to Alex Assaf and Zoe Watt from BG Group. We thank our colleagues at the International Centre for Carbonate Reservoirs (funded by BG Group and Petrobras) and at the Carbonate Reservoir Group at Heriot-Watt University, especially Mohamed Ahmed, for the stimulating discussions. We also acknowledge Schlumberger for providing access to Petrel and Eclipse and Geomodeling for access to SBED.

References

Aharonov, E., Laronne, B. L., Karcz, Z., Toussaint, R., Kadori, M. and Sagy, A. 2012. Large-scale distributions of sedimentary stylolites in carbonates: Field observations and emerging insights regarding evolution, strain and dissolution. AAPG Search and Discovery Article #120034, Proceedings of AAPG Hedberg Conference Fundamental Controls on Flow in Carbonates, Saint-Cyr Sur Mer, Provence, France, July 8-13, 2012.

Alsharhan, A.S. 1990. Geology and reservoir characteristics of Lower Cretaceous Kharaib Formation in Zakum Field, Abu Dhabi, United Arab Emirates. *In:* Brooks, J. (ed), *Classic Petroleum Provinces*. Geological Society Special Publications, **50**, 299–316.

Alsharhan, A.S. and Sadd, J. 2000. Stylolites in lower Cretaceous carbonate reservoirs. U.A.E. Society of Economic Paleontology and Mineralogy Special Publication, **69**, 185–207.

Brouste, A., Renard, F., Gratier, J. and Schmittbuhl, J. 2006. Variety of stylolites' morphologies and statistical characterisation of the amount of heterogeneities in the rock. *Journal of Structural Geology,* **29**, 422-434, doi:10.1016/j.jsg.2006.09.014.Chandra, V., Corbett, P.W.M., Hamdi, H. and Geiger, S. 2013. Improving Reservoir Characterisation and Simulation with Near Wellbore Modeling. *SPE Reservoir Evaluation & Engineering*, **16 (2)**,183-193, SPE Journal Paper 148104-PA.

Corbett, P. W.M., Anggraeni, S. and Bowen, D. 1999. The use of the probe permeameter in carbonates - addressing the problems of permeability support and stationarity. *The Log Analyst*, **40**, 316-326.

Dabek, L. B. and Knepp, R. 2011. Bioturbation and Its Effects on Permeability in Wave-Dominated Shoreface Rocks of the Spring Canyon Member, Blackhawk Formation, Utah, USA. AAPG Search and Discovery Article # 50425. Proceedings of AAPG Annual Convention and Exhibition, Houston, Texas, USA, April 10-13, 2011.

Deutsch C.V. and Journel A.G. 1998. GSLIB. Geostatistical Software Library and User's Guide. N.Y., Oxford University Press.

Deutsch C.V. 2002. Geostatistical Reservoir Modeling. Oxford University Press.

Dijk, P., Berkowitz, B. and Bendel, P. 1999. Investigation of flow in water-saturated rock fractures using nuclear magnetic resonance imaging (NMRI). *Water Resources Research*, **35(2)**, 347-360.

Ebner, M., Piazolo, S., Renard, F. and Koehn, D. 2010. Stylolite interfaces and surrounding matrix material: Nature and role of heterogeneities in roughness and microstructural development. *Journal of Structural Geology,* **32**, 1070-1084, doi:10.1016/j.jsg.2010.06.014.

Ehrenberg, S. N., Walderhaug, O. and Bjørlykke, K. 2012. Carbonate porosity creation by mesogenetic dissolution: Reality or illusion? AAPG Bulletin, **96 (2)**, 217–233.

Elfenbein, C., Ringrose,P. S. and Christie, M. 2005. Small-scale reservoir modeling tool optimizes recovery offshore Norway. World Oil, **226(10),** 45–50.

Esteban, M. and Taberner, C. 2002. Reconstructing fluid flow evolution from compressional to extensional regimes. Late corrosive fluids: a key factor for porosity formation and enlargement. *In:* Proceedings of AAPG Hedberg Conference, Austin, p.234.

Esteban, M. and Taberner, C. 2003. Secondary porosity development during late-burial in carbonate reservoirs as a result of mixing and/or cooling of brines. *Journal of Geochemical Exploration*, **78–79**, 355–359.

Goswami B. G., Singh H., Bhatnagar A. K., Sinha A. K. and Singh R. R. 2007. Petroleum Systems of the Mumbai Offshore Basin, India. AAPG Search and Discovery Article #10154. Proceedings of AAPG Annual Convention, Long Beach California, April 1-4, 2007.

Jameson, J. 1994. Models of Porosity Formation and Their Impact on Reservoir Description, Lisburne Field, Prudhoe Bay, Alaska, *AAPG Bulletin*, **78 (11)**, 1651–1678.

Koehn, D., Ebner, M., Renard, F., Toussaint, R. and Passchier, C. W. 2012. Modelling of stylolite geometries and stress scaling. *Earth and Planetary Science Letters,* **341–344**, 104–113, http://dx.doi.org/10.1016/j.epsl.2012.04.046.

Lambert, L., Durlet, C., Loreau, J. and Marnier, G. 2006. Burial dissolution of micrite in Middle East carbonate reservoirs (Jurassic–Cretaceous): keys for recognition and timing. *Marine and Petroleum Geology*, **23**, 79-92. Lucia, F. J. 1995. Rock-fabric/petrophysical classification of carbonate pore space for reservoir characterisation. *AAPG Bulletin*, **79 (9)**, 1275–1300.

Lucia, F. J. 1999. Carbonate Reservoir Characterisation. Springer, Germany.

Mazzullo, L.J. and Harris, EM. 1991. An overview of dissolution porosity development in the deep-burial environment, with examples from carbonate reservoirs in the Permian Basin. *In:* Candellaria, M.E (eds), *Permian Basin Plays--Tomorrow's Technology Today.* Geological Society Publication, **91-89**, 125-138.

Moshier, S.O. 1989. Development of microporosity in a micritic limestone reservoir, Lower Cretaceous, Middle East. *Sedimentary Geology,* **63**, 217–240.

Nordahl, K. 2004. *A petrophysical evaluation of tidal heterolithic deposits: application of a near wellbore model for reconciliation of scale dependent well data.* PhD thesis, Norwegian University of Science and Technology.

Nordahl, K., Ringrose, P.S. and Wen, R. 2005. Petrophysical characterisation of a heterolithic tidal reservoir interval using a process-based modeling tool. *Petroleum Geoscience*, **11(1)**, 17-28.

Oates, M., Mishra, G., Sultana, N. and Nath, G. 2012. Resolving a permeability mismatch in a mature carbonate field. Proceedings of SPE Oil and Gas India Conference and Exhibition, Mumbai, March 2012, SPE Paper 155458.

Peacock , D.C.P. and Azzam, I.N. 2006. Development and scaling relationships of a stylolite population. *Journal of Structural Geology*, **28**, 1883-1889, doi:10.1016/j.jsg.2006.04.008.

Pickup, G. E. and Sorbie, K. S. 1996. The scaleup of two-phase flow in porous media using phase permeability tensors. *SPE Journal*, **1**, 369-382.

Renard, F., J. Schmittbuhl, J. P. Gratier, P. Meakin. and E. Merino. 2004. Three-dimensional roughness of stylolites in limestones, *Journal of Geophysical Research*, **109**, B03209, doi:10.1029/2003JB002555.

Ringrose, P.S., Allard, W., Martinius and Jostein, A. 2008. Multiscale geological reservoir modeling in practice, Geological Society, London, Special Publications, **309**, 123-134, doi:10.1144/SP309.9

Sattler, U., Zampetti, V., Schlager, W.. and Immenhauser, A. 2004. Late leaching under deep burial conditions: a case study from the Miocene Zhujiang Carbonate Reservoir, South China Sea. *Marine and Petroleum Geology*, **21**, 977-992.

Wen, R., Martinius, A.W., Naess, A. and Ringrose, P.S. 1998. Three-dimensional simulation of small-scale heterogeneity in tidal deposits – a process-based stochastic method. Proceedings of 4th Annual Conference of the International Association of Mathematical Geology, Ischia De Frede, Naples, 129-134.

Witherspoon, P. A., Wang, J. S. Y., Iwai, K. and Gale, J. E. 1980. Validity of cubic law for fluid flow in a deformable rock fracture. *Water Resources Research*, **16**, 1016-1024.

Wright, V.P. and Barnett, A.J. 2011. Burial corrosion and porosity formation: from the seismic to micropore scale, but what processes do we blame? *Carbonate Geochemistry: Reactions and Processes in Aquifers and Reservoirs*. Karst Waters Institute Special Publication, **16**, 81-83.

List of figures

Fig. 1 Core data and permeability transform used for generating the original geomodel of Field X.

Fig. 2 Cumulative oil production curves from Well Group 1. OPT is the history matched simulation model, which aligns perfectly with the historic production data OPTH. OPT is considered as the base case for our work. OPT1 is the simulated production after removing horizontal K-multipliers from the zones. OPT2 is the simulated production after removing zone and local well K-multipliers. OPT3 is the simulated production after removing the well productivity multipliers in addition to the zone and well K-multipliers. STB is the abbreviation for ‘Stock Tank Barrels’.

Fig. 3 Gradual water-cut profile of Field X. Erratic water break-through was not observed during the field’s production life and hence fractures are probably not controlling fluid flow in the reservoir. The periods of zero water-cut correspond to the times when field production operations were temporarily suspended.

Fig. 4 Stratigraphic summary of Field X showing the main reservoir units A Zone and B Zone, the gas-oil contact (GOC) and the oil-water contact (OWC).

Fig. 5 Illustration of foraminifera distribution in the limestones of Field X with reference to a carbonate ramp model (modified from Wright & Barnett 2011). A Zone is dominated by the outer ramp *Nummilitides* while B Zone mainly consists of inner ramp *Coskinolina* facies. Facies key; CG- *Coskinolina* grainstones; CA- *Coskinolina* and *Alveolinid* facies; CH- *Coskinolina* hash facies; M- *Miliolid* facies; H- Hash facies with fine skeletal debris; N- *Nummulites* matrix-rich limestones, ND- *Nummulites-Discocyclinid* facies.

Fig. 6 Key paragenetic events that occurred in A Zone and B Zone (modified from Wright & Barnett 2011). The depositional facies underwent extensive early cementation followed by compaction and pressure solution developing stylolites and associated tension-gashes. This was followed by a major phase of dissolution associated with saddle dolomite and dickite precipitation.

Fig. 7 (**a**) Photomicrograph illustrating tectonic vein-filling calcite cement that has been corroded. (**b**) Deeply etched stylolites and associated tension-gashes observed in core. Pyrite precipitation is common. (**c**) Photomicrograph showing fractures with leached bladed calcite cement, saddle dolomite and dickite. Dickite is a type of kaolin mineral that indicates former activity of organic-rich acidic fluids. (**d**) Back-Scatter Electron Microscope (BSEM) image of typical corroded matrix with microporosity.

Fig. 8 Illustration of varying scales of solution-enhanced porosity caused by late-burial corrosion within the CEP zones in A and B Zones. (**a**) Vuggy/moldic porosity in core. (**b**) Leached stylolite and associated tension-gashes. (**c**) Matrix micro- and macro-porosity observed in thin-section.

Fig. 9 (**a**) Swarms of solution-enlarged stylolites (left) and associated small-scale tension-gashes (right) observed in core from Well Group 1. (**b**) Photomicrograph illustrating leached stylolite porosity.

Fig. 10 Porosity distribution of unmodified matrix and CEP zones, denoted by R1 and R2, respectively. The CEP zones (R2) exhibit higher porosity than the tight limestone (R1).

Fig.11 (**a**) Mini-permeameter map showing the distribution of permeability between the corroded and unmodified limestone matrix in the core. Note that core plugs were taken towards the tighter matrix. (**b**) Histogram of permeability distribution of unmodified matrix and CEP zones, denoted by R1 and R2, respectively. The CEP zones (R2) exhibit higher permeability range of than the tight limestone (R1).

Fig.12 Image logs correlated with core; dark coloured conductive matrix represents the corroded zones and light coloured resistive matrix the tight limestone

Fig.13 (**a**) Near-wellbore modelling template of stylolites in tight limestone matrix. (**b**) Near-wellbore modelling template of stylolites and associated leached tension-gashes surrounded by matrix macro-porosity. (**c**) Near-wellbore modelling template with stylolites and halos of matrix macro-porosity, mimicking the distribution of the solution-enhanced porosity in association with stylolites.

Fig. 14 Comparison of Field X core porosity and horizontal permeability data with Lucia's (1995 and 1999) permeability transforms and effective porosity and horizontal permeability values from the near-wellbore upscaling workflow. Note that the original core permeability-transform is closer to Lucia's class 3 transform, reflecting poor quality matrix. The upscaled properties obtained from the near-wellbore modelling are closer to the higher quality Lucia class 2 and 1 transforms.

Fig. 15 (**a**) Top-view of the field scale geomodel of Field X showing the porosity distribution and the approximate location of all the well groups (see arrows). The field scale geomodel comprises over five million grid blocks with cell dimensions of 50 m x 50 m horizontally. Cell sizes in the vertical direction have an average thickness of 2 m, enabling the resolution of reservoir layers and the capture of vertical heterogeneity. (**b**) Close-up showing the sector model containing Well Group 1 used for the simulation study. The location of the sector model is indicated by the grey shaded area in the field scale model. The colour scale for porosity is the same in the sector and in the field scale model.

Fig. 16 Cumulative oil production curves simulated for sector model containing Well Group1. Results are from all geomodel scenarios before and after incorporating facies R2. Note that base case and historic curves are overlapping. In Case 1, the K_v distribution from the base case was used for rock types R1 and R2. In Case 2 the K_v/K_h values estimated from the near-wellbore modelling and upscaling workflow were used for distributing K_v in rock type R2. STB is the abbreviation for 'Stock Tank Barrels'.

Fig. 17 Cumulative gas production curves simulated for the sector model containing Well Group1. Results are from all geomodel scenarios before and after incorporating facies R2. Note the divergence between the historic and base case profiles. MSCF is the abbreviation of 'Thousand Standard Cubic Feet'.

Fig. 18 Cumulative water production curves simulated for the sector model containing Well Group1. Results are from all geomodel scenarios before and after incorporating facies R2. Note that the base case and Case 1 profiles are overlapping. STB is the abbreviation for 'Stock Tank Barrels'.

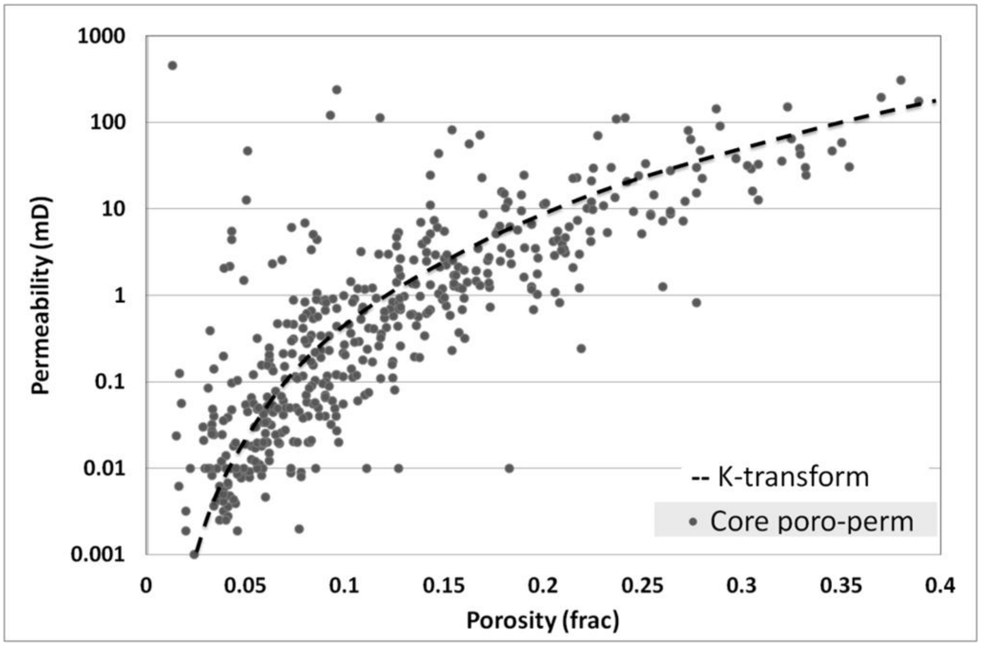

Fig. 1 Core data and permeability transform used for generating the original geomodel of Field X.

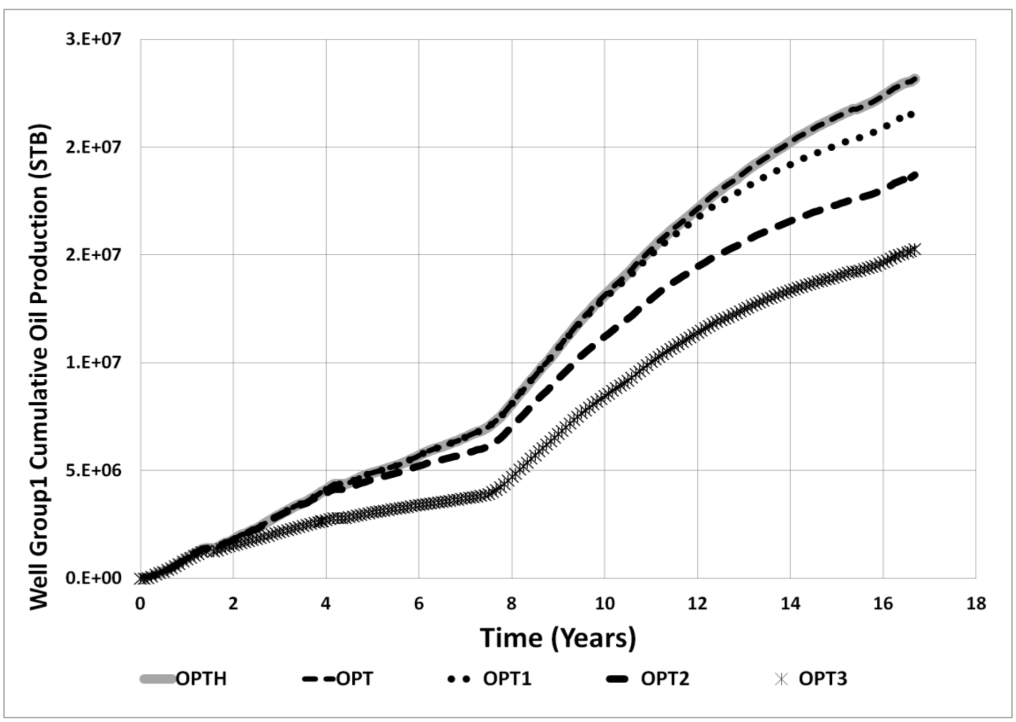

Fig. 2 Cumulative oil production curves from Well Group 1. OPT is the history matched simulation model, which aligns perfectly with the historic production data OPTH. OPT is considered as the base case for our work. OPT1 is the simulated production after removing horizontal K-multipliers from the zones. OPT2 is the simulated production after removing zone and local well K-multipliers. OPT3 is the simulated production after removing the well productivity multipliers in addition to the zone and well K-multipliers. STB is the abbreviation for 'Stock Tank Barrels'.

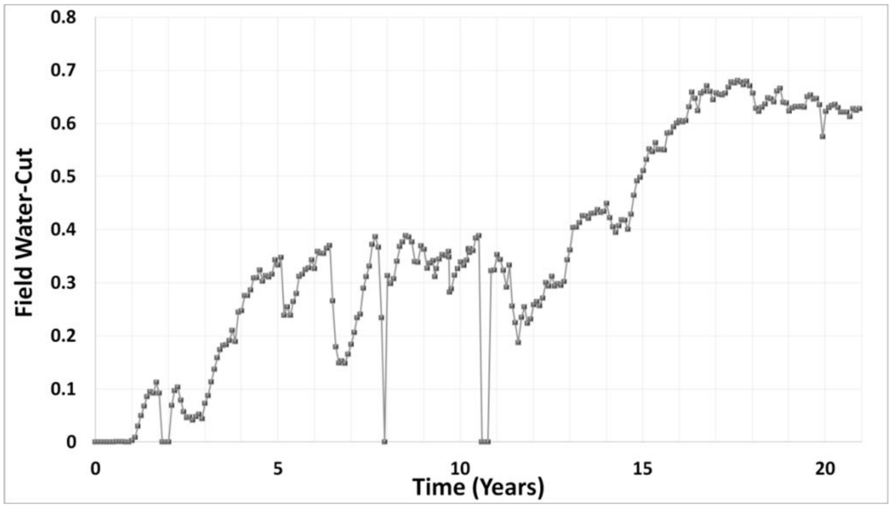

Fig. 3 Gradual water-cut profile of Field X. Erratic water break-through was not observed during the field's production life and hence fractures are probably not controlling fluid flow in the reservoir. The periods of zero water-cut correspond to the times when the field production operations were temporarily suspended.

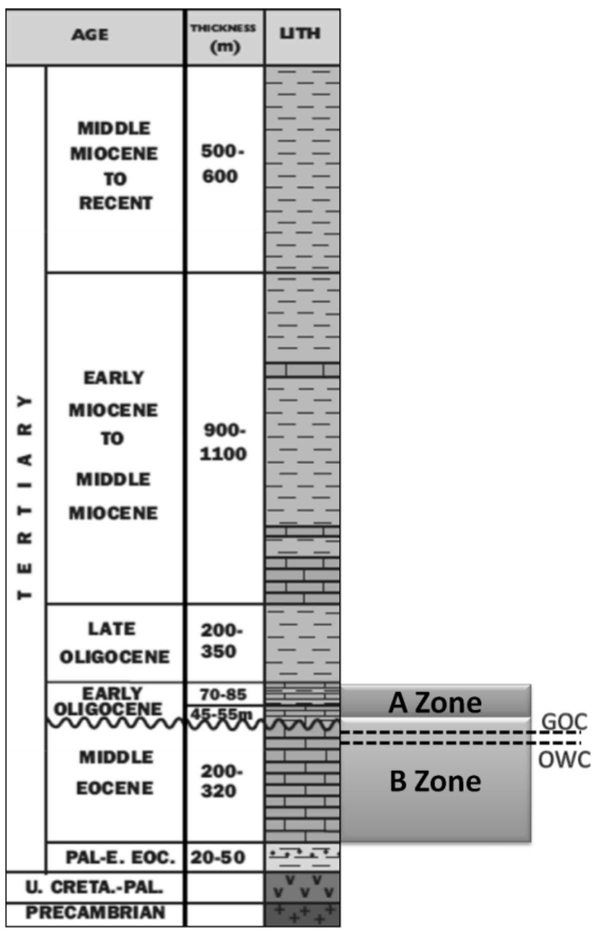

Fig. 4 Stratigraphic summary of Field X showing the main reservoir units A Zone and B Zone, the gas-oil contact (GOC) and the oil-water contact (OWC).

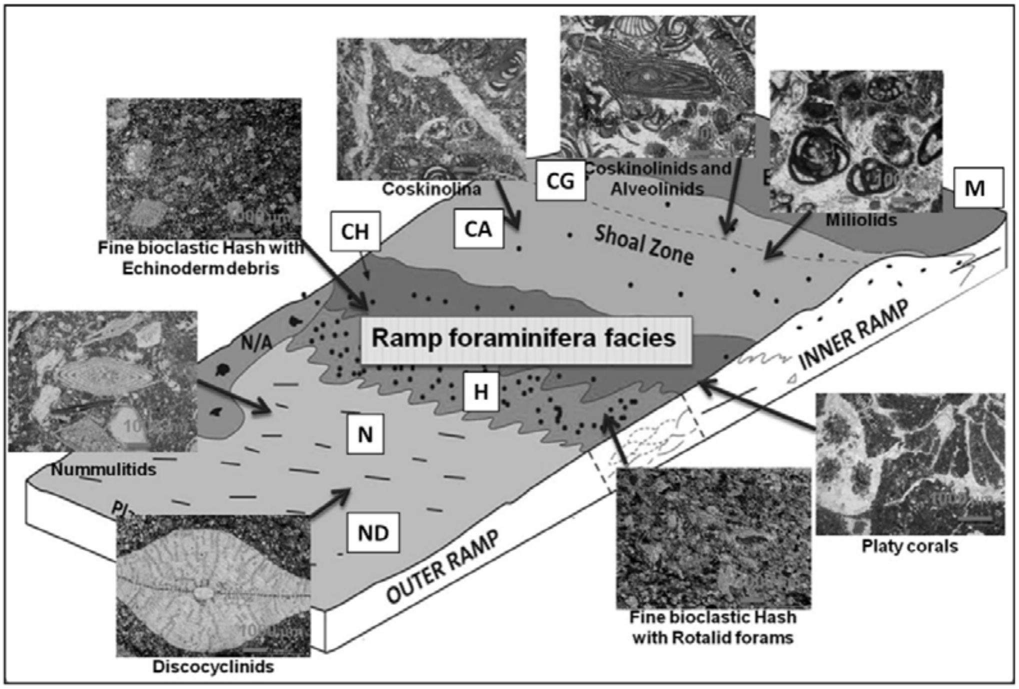

Fig. 5 Illustration of foraminifera distribution in the limestones of Field X with reference to a carbonate ramp model (modified from Wright & Barnett 2011). A Zone is dominated by the outer ramp *Nummilitides* while B Zone mainly consists of inner ramp *Coskinolina* facies. Facies key; CG- *Coskinolina* grainstones; CA- *Coskinolina* and *Alveolinid* facies; CH- *Coskinolina* hash facies; M- *Miliolid* facies; H- Hash facies with fine skeletal debris; N- *Nummulites* matrix-rich limestones, ND- *Nummulites*-*Discocyclinid* facies.

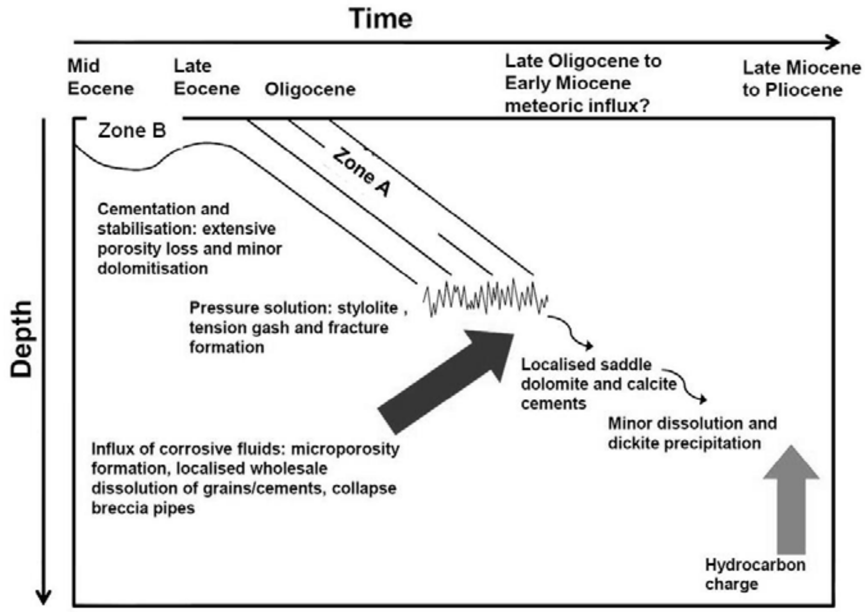

Fig. 6 Key paragenetic events that occurred in A Zone and B Zone (modified from Wright & Barnett 2011). The depositional facies underwent extensive early cementation followed by compaction and pressure solution developing stylolites and associated tension-gashes. This was followed by a major phase of dissolution associated with saddle dolomite and dickite precipitation.

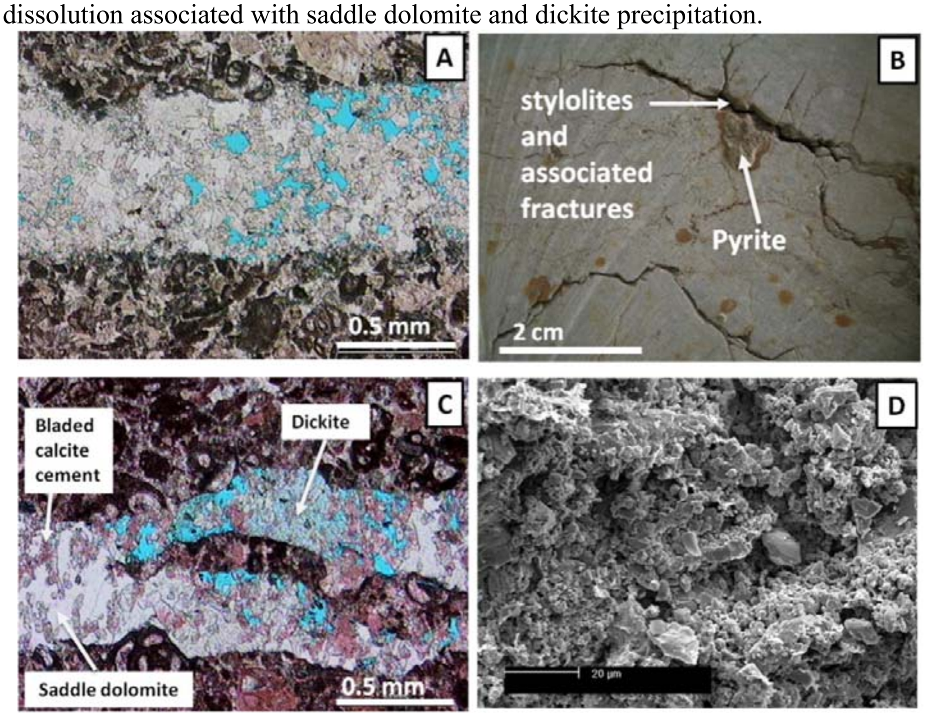

Fig. 7 (**a**) Photomicrograph illustrating tectonic vein-filling calcite cement that has been corroded. (**b**) Deeply etched stylolites and associated tension-gashes observed in core. Pyrite precipitation is common. (**c**) Photomicrograph showing fractures with leached bladed calcite cement, saddle dolomite and dickite. Dickite is a type of kaolin mineral that indicates former activity of organic-rich acidic fluids. (**d**) Back-Scatter Electron Microscope (BSEM) image of typical corroded matrix with microporosity.

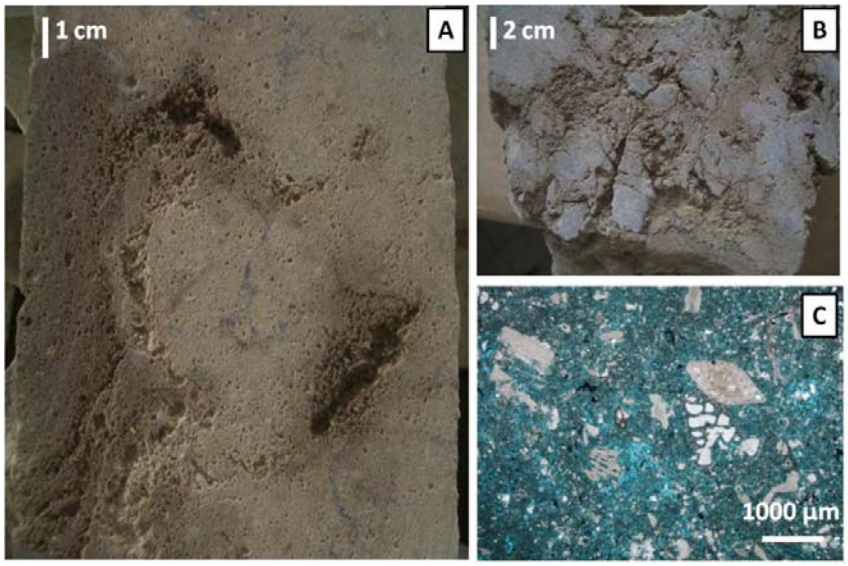

Fig. 8 Illustration of varying scales of solution-enhanced porosity caused by late-burial corrosion within the CEP zones in A and B Zones. (**a**) Vuggy/moldic porosity in core. (**b**) Leached stylolite and associated tension-gashes. (**c**) Matrix micro- and macro-porosity observed in thin-section.

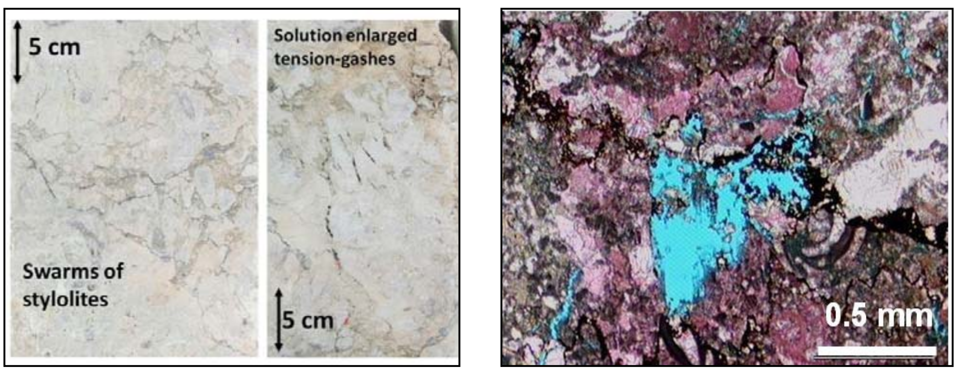

(a) (b)

Fig. 9 (**a**) Swarms of solution-enlarged stylolites (left) and associated small-scale tension-gashes (right) observed in core from Well Group 1. (**b**) Photomicrograph illustrating leached stylolite porosity.

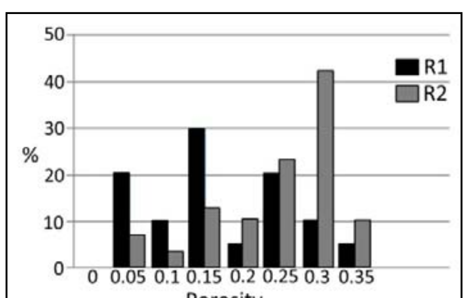

Fig. 10 Porosity distribution of unmodified matrix and CEP zones, denoted by R1 and R2, respectively. The CEP zones (R2) exhibit higher porosity than the tight limestone (R1).

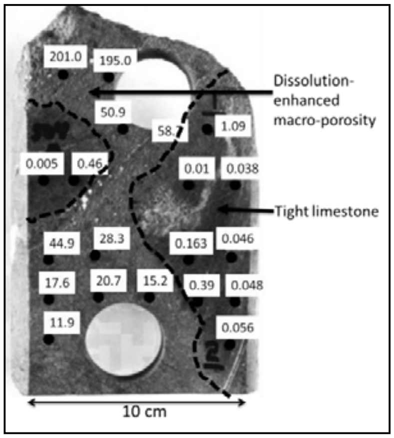

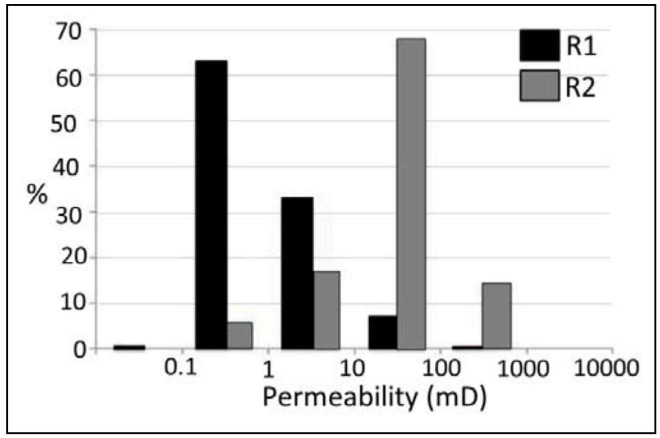

(a) (b)

Fig.11 (**a**) Mini-permeameter map showing the distribution of permeability between the corroded and unmodified limestone matrix in the core. Note that core plugs were taken towards the tighter matrix. (**b**) Histogram of permeability distribution of unmodified matrix and CEP zones, denoted by R1 and R2, respectively. The CEP zones (R2) exhibit higher permeability range of than the tight limestone (R1).

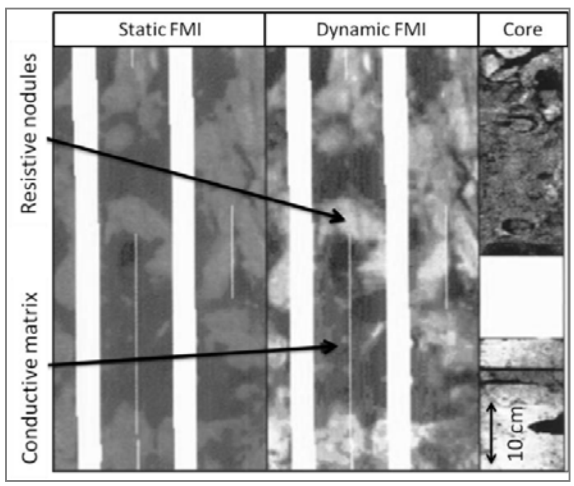

Fig.12 Image logs correlated with core; dark coloured conductive matrix represents the corroded zones and light coloured resistive matrix the tight limestone.

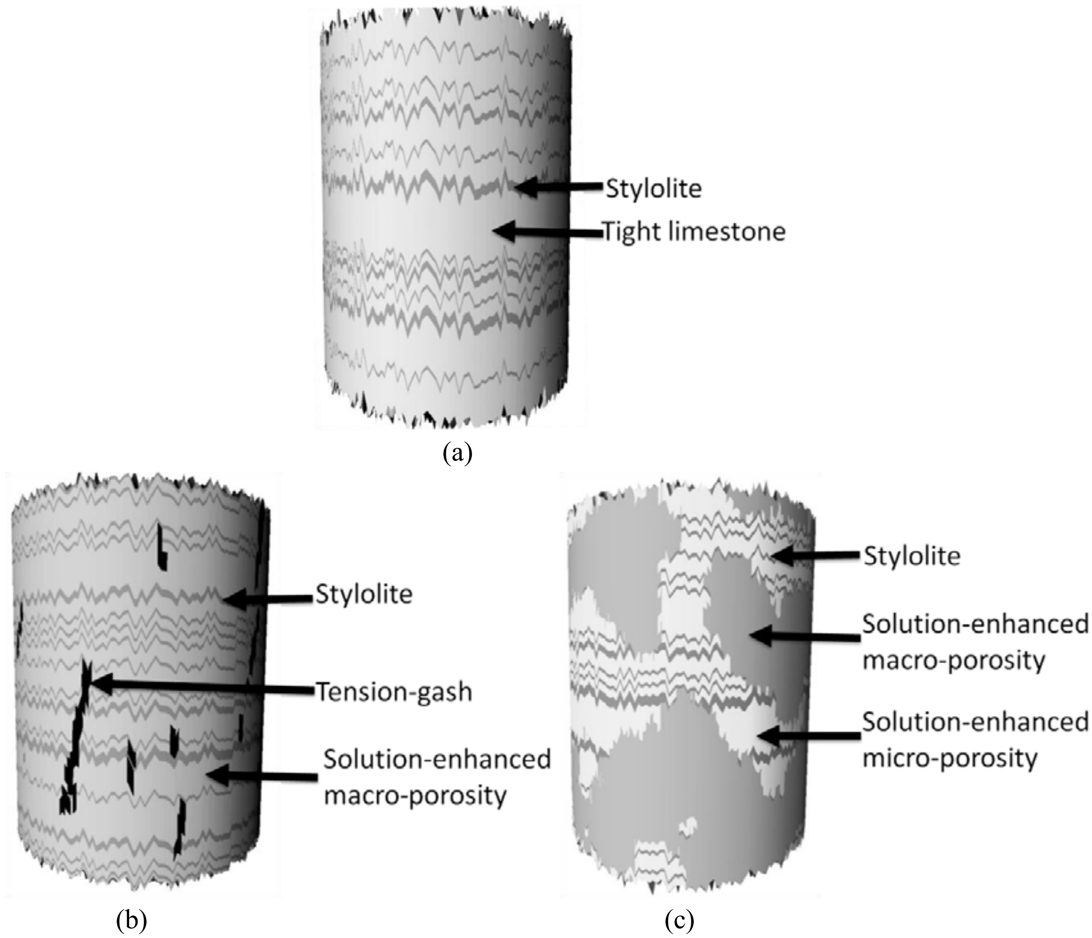

Fig.13 (**a**) Near-wellbore modelling template of stylolites in tight limestone matrix. (**b**) Near-wellbore modelling template of stylolites and associated leached tension-gashes surrounded by matrix macro-porosity. (**c**) Near-wellbore modelling template with stylolites and halos of matrix macro-porosity, mimicking the distribution of the solution-enhanced porosity in association with stylolites.

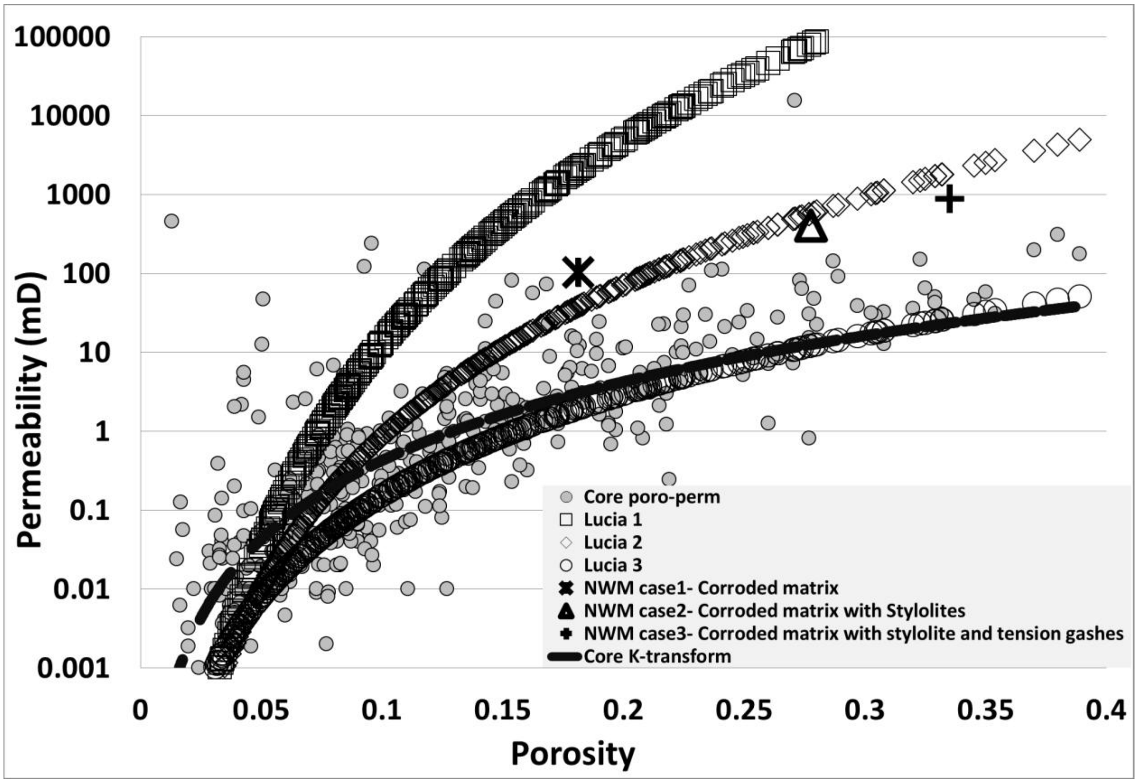

Fig. 14 Comparison of Field X core porosity and horizontal permeability data with Lucia's (1995 and 1999) permeability transforms and effective porosity and horizontal permeability values from the near-wellbore upscaling workflow. Note that the original core permeability-transform is closer to Lucia's class 3 transform, reflecting poor quality matrix. The upscaled properties obtained from the near-wellbore modelling are closer to the higher quality Lucia class 2 and 1 transforms.

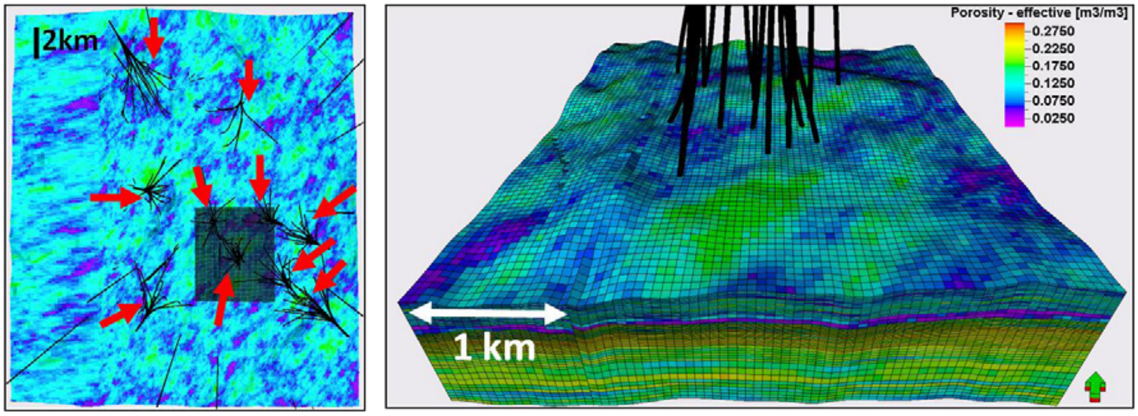

(a) (b)

Fig. 15 (**a**) Top-view of the field scale geomodel of Field X showing the porosity distribution and the approximate location of all the well groups (see arrows). The field scale geomodel comprises over five million grid blocks with cell dimensions of 50 m x 50 m horizontally. Cell sizes in the vertical direction have an average thickness of 2 m, enabling the resolution of reservoir layers and the capture of vertical heterogeneity. (**b**) Close-up showing the sector model containing Well Group 1 used for the simulation study. The location of the sector model is indicated by the grey shaded area in the field scale model. The colour scale for porosity is the same in the sector and in the field scale model.

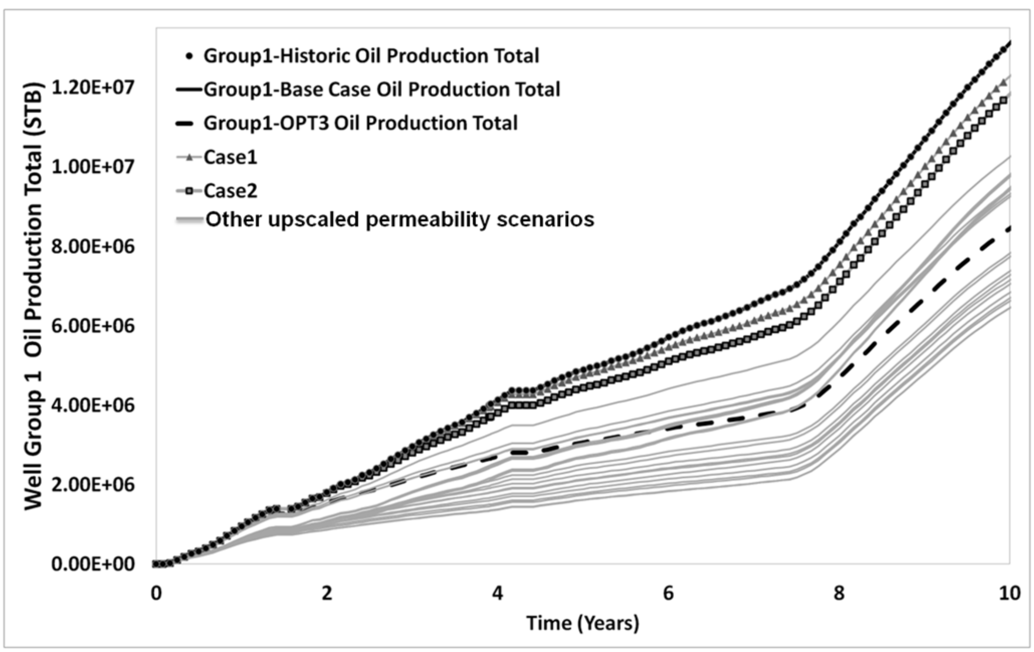

Fig. 16 Cumulative oil production curves simulated for sector model containing Well Group1. Results are from all geomodel scenarios before and after incorporating facies R2. Note that base case and historic curves are overlapping. In Case 1, the K_v distribution from the base case was used for rock types R1 and R2. In Case 2 the K_v/K_h values estimated from the near-wellbore modelling and upscaling workflow were used for distributing K_v in rock type R2. STB is the abbreviation for 'Stock Tank Barrels'.

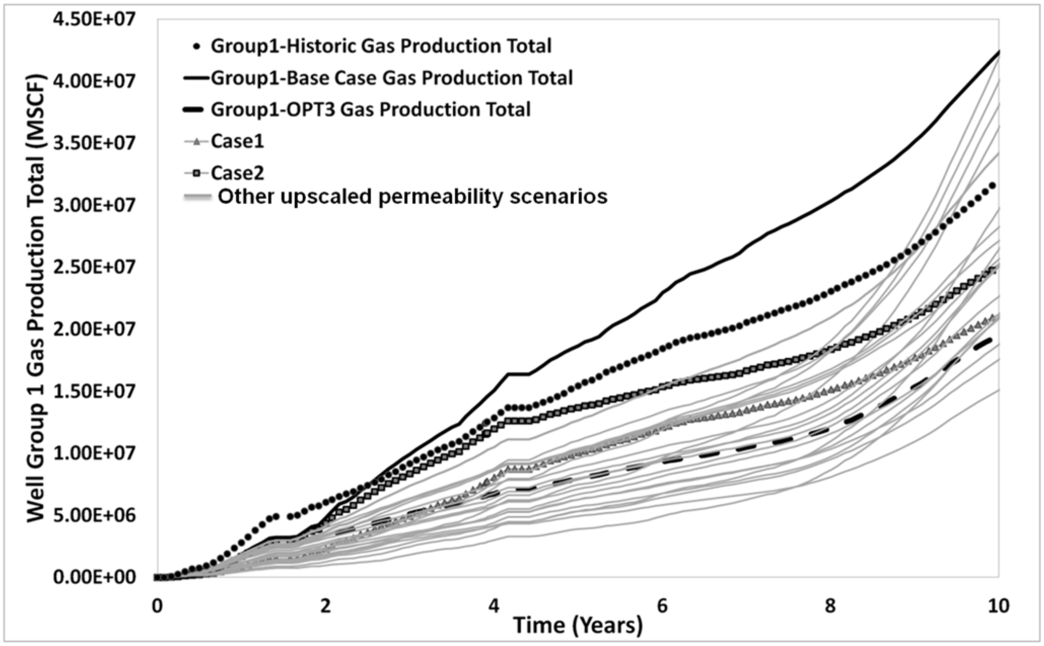

Fig. 17 Cumulative gas production curves simulated for the sector model containing Well Group1. Results are from all geomodel scenarios before and after incorporating facies R2. Note the divergence between the historic and base case profiles. MSCF is the abbreviation of 'Thousand Standard Cubic Feet'.

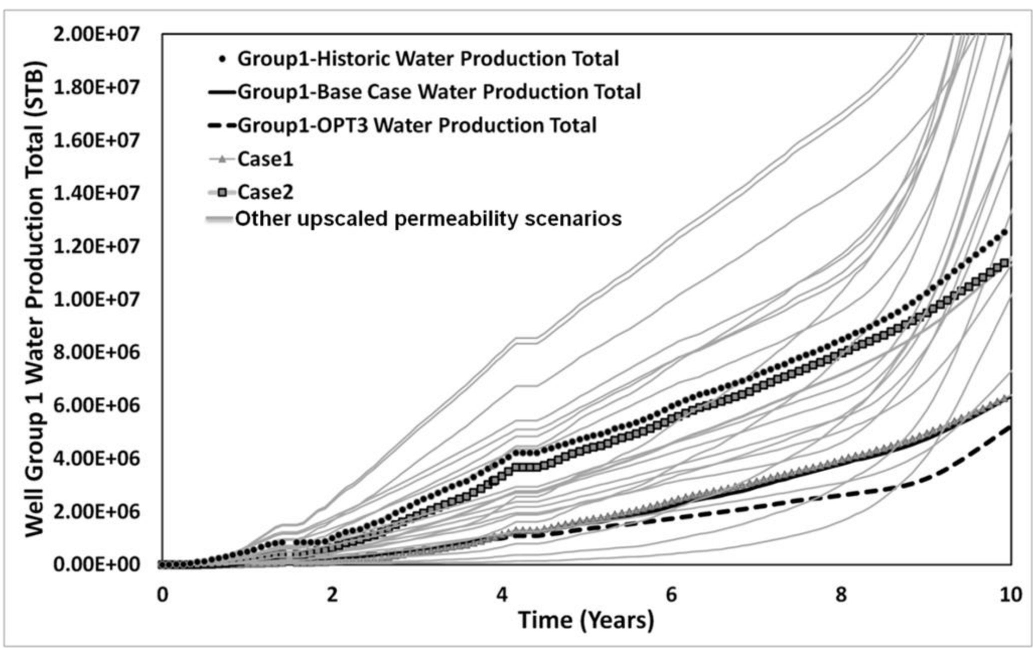

Fig. 18 Cumulative water production curves simulated for the sector model containing Well Group1. Results are from all geomodel scenarios before and after incorporating facies R2. Note that the base case and Case 1 profiles are overlapping. STB is the abbreviation for 'Stock Tank Barrels'.

Table 1. *Summary of petrophysical data analysis*

Scale	Available data	Resolution	Depth of Investigation	Key Geological Heterogeneities Resolved	Petrophysical Property Inferred
Pore	SCAL-MICP analysis	-	-	- Corrosion enhanced patchy microporosity - Microstylolites - Depositional facies	- Pc, Kr - Pore throat diameter range - Pore size distribution - Macro-Micro-porosity cut-offs
	Thin section images	Few µm-mm	Few mm		
Core	Probe-permeability	Few mm-cm	Few mm-cm	- Depositional facies - Corrosion enhanced matrix meso- and macro- porosities - Vuggy/moldic porosity - Corrosion enhanced stylolites and tension-gashes - Stylobreccia	- Matrix porosity distribution range - Core scale poro-perm transfoms - Core scale flow zone indicators (FZI)
	RCA- Plug poro-perm	5 cm	5 cm		
	Core plug XRT	Few cm	Few cm		
	Core SGR	Few cm	Few cm		
	Core description logs	mm- m	Upto 10 cm		
Wireline	Wellbore image Logs	0.5 cm	2.5 cm	- A/B unconformity - Shaly zones - Fractures/stylolites captured in image log resolution	- Total and Effective porosities - Initial water saturation model - STOIIP calculations
	Density	46 cm	13 cm		
	Neutron porosity	30 cm	23 cm		
	Gamma	30.5 cm	61 cm		
	Deep resistivity	46 cm	81 cm		

Table 2. *Poro-perm range of CEP zones from RCA data*

CEP type	Porosity (frac)			Permeability (mD)		
	Min	Max	Mean	Min	Max	Mean
Matrix-micro porosity	0.04	0.15	0.08	0.001	7.28	0.4
Matrix-macro porosity halos near stylolites	0.12	0.4	0.23	100	700	300
Micro-porosity halo near stylolites	0.08	0.2	0.12	15	120	50
Leached stylolites	0.4	0.8	0.5	500	2500	1000
Leached tension-gashes	0.4	0.8	0.5	5000	25000	10000

Table 3. *Effective poro-perm of CEP zones from near-wellbore upscaling*

CEP Zone scenario	Φ_{eff}	K_{h-eff}	K_{v-eff}/K_{h-eff}
Corroded matrix with micro- and macro-porosity	0.23	250	1
Corroded matrix with leached stylolites	0.3	600	1.5
Corroded matrix with leached tension-gashes	0.26	300	2
Corroded matrix with leached stylolites and tension-gashes	0.35	900	2.5